Title
The Effect of Sand Gradation on the Dynamic Performance of Embankments

Author
Love, Nathan C.

Publication Date
2022

Peer reviewed|Thesis/dissertation

The Effect of Sand Gradation on the Dynamic Performance of Embankments

By

NATHAN LOVE
THESIS

Submitted in partial satisfaction of the requirements for the degree of

MASTER OF SCIENCE

in

Civil and Environmental Engineering

in the

OFFICE OF GRADUATE STUDIES

of the

UNIVERSITY OF CALIFORNIA

DAVIS

Approved:

Jason T. DeJong, Chair

Katerina Ziotopoulou

Alejandro Martinez

Committee in Charge

2022

To the King of ages, immortal, invisible, the only God, be honor and glory forever and ever. Amen. (1 Timothy 1:17)

ABSTRACT

Researchers have recently explored the effects of gradation on earthquake-induced liquefaction behavior, showing that broadly graded sands have a distinct response compared to poorly graded sands. However, current state of practice applies liquefaction procedures developed from poorly graded sands to liquefiable natural alluvial deposits that are much more broadly graded. The goal of this research is to better understand and quantify the systematic effects of sand gradation on embankment performance and the consequences of liquefaction. The soil's coefficient of uniformity (C_u) is used as a proxy for gradation as it is a single parameter that affects multiple index and density metrics, which in turn generate distinct responses.

The testing series evaluated herein incorporates results from two centrifuge tests, including four different soil types with C_u values ranging from 2 to 12. The centrifuge testing was performed on the 9 m-radius centrifuge at the Center for Geotechnical Modeling (CGM) at UC Davis. The model container was designed with two identical parallel sloping embankments of different gradations, prepared to the same relative density (D_r) of 40%, and configured with arrays of accelerometers and pore pressure transducers. High speed cameras mounted outside the model container recorded embankment plane-strain deformations of dyed soil columns through the clear polycarbonate sidewalls. The models were subjected to four strong motion events of increasing intensity. The results reveal that at the same relative density, horizontal displacements and, strains decreased by over 50% with increasing C_u, whereas settlements reduced to zero and even resulted in net upward displacement due to the strong dilatancy of the broadly graded sands. Despite similar numbers of cycles to liquefaction triggering, the rate of dissipation of excess pore pressures occurred 3-4 times faster for the more broadly graded sands, reducing the duration of soil matrix instability. The accelerations in the broadly graded embankments were also approximately 3 times

more amplified than the poorly graded embankments. Together, these results show that gradation plays a significant role in the consequences that proceed from liquefaction triggering, which should be explicitly considered in the evaluation of liquefaction susceptibility and consequences.

TABLE OF CONTENTS

1 INTRODUCTION

Do the liquefaction triggering and deformation procedures used in earthquake engineering practice reasonably estimate the consequences of liquefaction in broadly graded sands, and if not, to what degree does gradation affect performance during an earthquake? The first part of this question has been explored in recent years (Sturm 2019, Rollins et al. 2021, Carey et al. 2022a, Dhakal et al. 2022, Ruttithivaphanich and Sasanakul 2022), and results collectively indicate that the effects of gradation are not adequately captured in the liquefaction triggering procedures currently used in practice. The goal of the testing program presented herein is to address the second half of this question and elucidate the effect of the coefficient of uniformity (C_u) on embankment performance and the consequences of liquefaction at a fixed relative density (D_r) = 40%. Herein liquefaction is defined as an excess porewater pressure ratio (r_u) = 1.

The liquefaction case history databases used to develop the triggering and deformation procedures used in practice today predominantly contain observations of sites consisting of poorly graded clean sands (e.g. Idriss and Boulanger 2004). While there have been many observations of destructive liquefaction in poorly graded sands, there are also numerous examples of broadly graded sands and gravels that have liquefied (e.g., 2008 Wenchuan Earthquake). These liquefiable alluvial deposits commonly found in nature are more broadly graded with C_u values greater than 30 (Sturm and DeJong 2022). Yet, the state of practice is to input penetration resistance data from Standard Penetration Tests (SPT) or Cone Penetration Tests (CPT) from soil composed of broadly graded sands into the curves developed based on poorly graded sands. This implicitly assumes either that penetration resistance and dynamic response are essentially the same for poorly graded sands and broadly graded sands, or that the penetration resistance adequately captures the changes

in physical, index, and mechanical properties for sands of varying gradation (Sturm and DeJong 2022).

The authors' research group has been addressing this uncertainty over recent years, finding that as a soil becomes more broadly graded, there can be distinct differences in soil properties, characterization measurements, and dynamic behavior. Centrifuge experiments by Sturm (2019) using a 1 m-radius centrifuge with level-ground conditions indicated that, "cone penetration resistance (q_c) measured in gravelly soils is unique from clean sands as a result of the increased potential for a compromised failure mechanism [due to a particle-to-probe size ratio less than 5] and the differences in mechanical properties between the two soil types" (Sturm 2019). Sturm (2019) developed a method to correct q_c for the particle-to-probe effect, but there remained a distinction in tip resistance profiles due to differences in mechanical properties. Sturm's level-ground experiments (2019) also demonstrated that the broadly graded soils exhibited increased dilation, which reduced cumulative volumetric strains. Further research by Carey et al. (2022a) testing gently sloped embankments in a 9 m-radius large centrifuge revealed increased dilation with broadening gradation and showed that while both the poorly graded sand and broadly graded embankments reached an $r_u = 1$, the broadly graded embankment displaced much less than its poorly graded counterpart, despite being built to the same target relative density (Carey et al. 2022a). Fundamental material differences have also been observed in the lab setting with triaxial testing, which shows that as C_u increases, the index void ratio values decrease, the critical state stress ratio (M, in q-p' space) increases slightly, compressibility decreases, and at the same state parameter dilatancy increases (Ahmed et al., 2022).

Others have also studied the effects of gradation, with an emphasis on the effect of gravel-sized particles. Dhakal et al. (2022) applied the poorly graded clean sands approach to a case

history of reclaimed gravels with particle sizes ranging from silts to gravels, highlighting the importance of considering soil composition and the dominant soil fraction of the soil matrix. Rollins et al. (2021) proposed new probabilistic liquefaction triggering curves for gravelly soils based on the Dynamic Cone Penetration Test (DPT). Wang et al. (2021) developed a skeleton void ratio for gravelly sand mixtures to determine the CSL. Ruttithivaphanich and Sasanakul (2022) conducted centrifuge testing on a mixture of 50% sand and 50% gravel, showing consistent results and observations as Carey et al. (2022).

With the importance of soil gradation having been established in relation to liquefaction evaluation, the authors' efforts shifted to determine the systematic effect of C_u on the system-level performance of embankments. C_u is used to quantify gradation, as it is easy to measure and is a single parameter that affects multiple index and density metrics, which in turn produce unique responses. However, C_u is a soil metric not without limitations. For example, a significantly gap-graded soil with a high C_u value would not benefit from the dense particle packing typically obtained from a broadly graded soil more commonly found in natural alluvial deposits. This could lead to a different performance than the broadly graded soils with larger C_u values discussed herein. However, the sands tested herein are generally representative of the more gradual gradations commonly deposited in nature.

Centrifuge testing was selected to investigate the systematic effect of C_u on the system-level performance of embankments. While laboratory testing such as direct simple shear or triaxial testing can reasonably approximate the element-level behavior of soils, it cannot capture how the soil impacts system performance. Numerical simulations cannot be utilized initially, as there is no data to validate the models. Centrifuge testing remains a preferred option, and more specifically the large 9 m-radius centrifuge at UC Davis is well-suited as the container is large enough to

minimize boundary effects and reasonably approximate field conditions under gravitational scaling.

The experimental program was designed for and tested using the 9 m-radius centrifuge at the Center for Geotechnical Modeling at UC Davis and consisted of two tests with identical designs, with four sands whose C_u values spanned from 2 to 12. The model was designed for a rigid container with clear container sidewalls and consisted of two parallel submerged sloping embankments, divided by a longitudinal aluminum wall, prepared to the same target relative density, and with each embankment comprised of a different sand. The models were characterized with cone penetration tests (CPTs) to determine relative density and bender elements to measure shear wave velocities. The models were shaken with a 1-Hz sinewave motion. There are four phases of interest for evaluating the response: pre-triggering shaking, post-triggering shaking at full motion amplitude (likely undrained), post-triggering shaking during motion amplitude decay (potentially partially drained), and post-shaking dissipation and reconsolidation.

Embankment response was recorded with accelerometers and pore pressure transducers, while high-speed cameras captured embankment deformations from the outside of the model containers, looking through the clear container sidewalls. The accelerometers reveal differences in embankment stiffnesses and amplification through the soil profile. The pore pressure transducers allow for continuous monitoring of liquefaction triggering ($r_u = 1$) and evolution of excess pore pressures throughout shaking and post-shaking dissipation and reconsolidation. De-liquefaction, where large strain cycles cause a temporary solidification of soil due to the dilatancy of the sand (Kutter and Wilson 1999), is observed in the excess pore pressure response as a rapid reduction in excess pore pressures. The high-speed cameras enable tracking of dynamic and permanent embankment displacements that can then be converted to embankment strains. Vertical settlements

due to liquefaction develop predominantly from: 1) shear-induced displacements of the soil associated with lateral spreading, or 2) post-liquefaction reconsolidation (Idriss and Boulanger 2008). Tracking vertical settlements facilitate a comparison of the embankments dilative nature and the source of settlements.

The data used in this paper are a synthesis of data from a previous centrifuge experiment that tested sands with a C_u of 2 and 8 (Carey et al. 2022a and Carey et al. 2022b) in addition to an original set of data from the authors from a model with more broadly graded sands with C_u values of 4 and 12, herein collectively referred to as the testing series. The two test designs were identical, apart from the sands tested.

2 SAND PROPERTIES

The testing program compares four sand mixtures with final C_u values between 2 and 12 and were created from source sands that are commercially available. For consistency in nomenclature and ease of reading, the sands will be named in the following format for this publication: "[integer C_u value]CU". Three of the mixtures, sands 2CU (100A), 4CU (33ABC), and 8CU (25ABCD), were originally developed by Sturm (2019). The fourth sand, with the largest C_u value, 12CU, was created for this testing series to extend the range of gradations. The details of the source sands are provided in Table 1, along with the percent by mass contained in each mixture. The uniform sand mixture properties are listed in Table 2. The Grain Size Distribution (GSD) plot for the soils is shown in Fig. 1. Apart from the 12CU, all the sands are poorly graded according to USCS classification.

The maximum void ratios (e_{max}) and minimum void ratios (e_{min}) of the sands were measured following ASTM standards. To measure e_{max} and e_{min}, Method A of ASTM D4254-16 (2016) and Method 1B of ASTM D4253-16 (2016) were used, respectively. The resulting values

are recorded in Table 2. Fig. 2 presents the void ratio extrema as a function of C_u for this test along with data from a larger database of high-quality void ratios tests of natural soils (Sturm and DeJong 2022). Also plotted are the target void ratios of the model at D_r = 40% using the colored data points. Generally, as C_u increases, the sand's void ratio extrema decrease due to greater particle packing efficiencies. This trend is consistent with the broader set of void ratios compiled by Sturm and DeJong (2022). The data also shows that the void ratios stabilize beyond a value of $C_u > 30$ due to a saturation of packing efficiencies. It is important to note that the void ratio extrema for the sands used in this study are representative of the broader set of in-situ soils and that the tested sands cover approximately 80% of the range of void ratios recorded in the natural sands.

With the critical state lines (CSL) defined from triaxial testing, the initial state parameters of the sands were estimated for the target relative density. Various forms of the state parameter (ξ) have been used as an index for a sand's liquefaction potential (Been and Jefferies 1985, Konrad 1988, Idriss and Boulanger 2003). The calculation of ξ requires the void ratios at the CSL and at the as-built relative density. The critical state lines are defined in both q-p' and e-log p' spaces by Ahmed et al. (2022). With the void ratios at the target D_r of 40%, the ξ (Been and Jefferies 1985) and relative state parameters (ξ_R) (Konrad 1988) were calculated and listed in Table 2. ξ increases slightly, from -0.096 to -0.067, as the C_u increases from 2 to 12, while ξ_R ranges from -0.32 to -0.38.

Permeabilities were directly measured at the target D_r and were similar for all sands. Permeabilities were measured with a constant head permeameter, following the procedures developed by Cimini (2016) and implemented by Shepard (2018), modified from ASTM 2434-68 (2006). The results are listed in Table 2. The permeabilities range from 0.025 to 0.031 cm/s. Permeability is controlled by the pore sizes, which is a combination of the soils 10^{th} percentile

particle size (D_{10}) and the void ratio. A slight increase in D_{10}, balanced by a reduction in void ratio resulted in these similar permeability values. Carey et al. and the authors designed the soil gradations so that the permeabilities were similar, which then allowed differences in the generation or dissipation of excess pore pressures (Δu) to be attributed to other soil properties or behavior. Permeabilities were also measured for dense and super loose (i.e. close to e_{min}) specimens. Additional figures on the effect of C_u on permeability are provided in the supplemental materials section.

3 EXPERIMENTAL SETUP AND MODEL CHARACTERIZATION

The experimental setup for the test of 4CU and 12CU is identical to that used in the prior 2CU and 8CU test reported by Carey et al. (2022a). More details are available in the data reports and past publications (Carey et al. 2022a, Carey et al. 2022b, Carey et al. 2022c, Love et al. 2022).

The embankments were constructed in layers via dry air pluviation (Sturm 2019). A schematic of the model geometry including sensor and probe locations is shown in Fig. 3a. At the base of the model, there was a 50 mm layer of dense (D_r > 90%) 2CU sand that was vibro-densified into place with a steel plate and hand-held vibrating compactor. The dense sand layer elevated the embankments into view of the high-speed cameras positioned outside the model container and was prepared dense to reduce susceptibility to liquefaction. Embankment sand was placed at a target D_r of 40% in a series of lifts that were vacuumed flat to 25 mm thickness. The final slope geometry was shaped with the vacuum and wooden guides and confirmed to be within 1 mm of the targeted depths.

Embankments were instrumented with arrays of horizontal accelerometers, pore pressure transducers, and bender elements. Sensors were individually calibrated and tested before being placed. Sensors were placed in the model after the lift was vacuumed flat and positioned within

+/- 1 mm of the target locations shown in Fig. 3a. The one-dimensional horizontal accelerometers were placed parallel to the shaking direction with the sensor head facing down-slope (+ acceleration), while pore pressure transducers were oriented perpendicular to the direction of shaking to minimize noise from reflected waves in the model container. A service loop in the down-slope direction was added in the sensor wire to allow slack for down-slope movement, minimizing potential slope reinforcement from sensor wires.

The embankments were saturated under vacuum (~95 kPa), with the pore fluid viscosity scaled to match the dynamic and diffusive time scales. The pore fluid was a mixture of water, Hydroxypropyl Methylcellulose (HPMC), and acid. The HPMC is a viscoelastic polymer thickening agent that was used to increase the viscosity of water. Approximately 2% by mass of HPMC was added to increase the viscosity of water by 40-times (40 mPa·s), to align the dynamic and diffusive time scales according to conventional scaling laws (Garnier et al. 2007). The fluid was measured to be within +/- 1 mPa·s of the target viscosity before model saturation. The container was flushed with CO_2 and inclined 5 degrees (with the head of the slope elevated) during saturation to ensure that a uniform saturation front progressed up the slope. Combined, the CO_2 and model inclination reduced the likelihood of air pockets being trapped in the embankment and promoted uniform model saturation. Three 6.35 mm holes along the height of the dividing wall equalized pressure and height of pore fluid across the two halves of the model.

Embankment cross-sectional displacements were recorded through the clear container sidewalls with arrays of high-speed cameras while images were post-processed with particle image velocimetry (PIV) software. Fig. 3b (reproduced from Carey et al. 2022a) illustrates the camera system configuration. Three high-speed cameras were positioned along the model container sidewalls at a distance of 31 cm and situated to record the embankment head, slope, and toe, with

overlapping fields of view. Columns of black sand were used as visual markers to track embankment deformations. The high contrast of the sand columns with the surrounding soil enabled accurate tracking of displacements. The black sand columns were formed with a mixture of water-soluble glue and dyed 2CU sand. When saturated, the columns softened and deformed with the embankments. An overlay of the black sand columns and their locations in the model cross section is seen in Fig. 3a; notice that two columns align with the sensor array locations projected to the sidewall. Indirect lighting was position above and below the embankments to view the embankment while minimizing glare in the images. The images captured by the high-speed cameras were processed using PIV software, GEOPIV-RG (Stanier et al. 2016), to obtain the location time histories of the black sand columns. Love et al. (2022) provides more information on the image capturing setup and analysis methods.

Each model container was subjected to four strong shaking events of increasing intensity. Fig. 3c shows the acceleration time histories of the applied base motions. Shakes 1-3 had different numbers of cycles, while Shake 4 had the same number of cycles as the third, at twice the amplitude. The resulting peak ground accelerations (PGA) and Arias intensities (Ia) for the four shaking events are shown in Table 3. This paper will mainly focus on the first three motions for which the initial embankment geometries largely remained the same.

The models were characterized with bender elements to measure the in-situ shear wave velocity (V_s) to approximate the small-strain shear modulus (G_{max}). Bender elements were placed at two depths in the model at effective stresses close to 45 kPa and 90 kPa. The bender elements experienced a malfunction with the data acquisition system during the test with 2CU and 8CU, thus a direct comparison of stiffness as a function of C_u is not feasible. However, the results from 4CU and 12CU are consistent with a previous test on 2CU and 8CU at D_r = 63% (Carey et al.

2022), which collectively indicate that shear stiffnesses increases with C_u for this set of soils. The V_s measurements and G_{max} estimations ($G_{max} = \rho \cdot V_s^2$) at about 90 kPa overburden stress are provided in Table 4. In both tests, V_s increases by 15-20% between the two soils. The increase in V_s is compounded by the increase in mass density, which combine to result in a 40-60% increase in G_{max} between the soils. These results are consistent with previously observed increases in shear stiffness due to a combination of a lower void ratio, larger D_{50}, and offset by an increase in C_u (Menq 2003, Sturm 2019). This is not to say that C_u is the only parameter that effects shear stiffness, nor that it effects it proportionally. The equation by Menq (2003) shows that G_{max} is inversely related to Cu, but it is the lower void ratio and larger D_{50} that outweigh the C_u with these soils.

CPTs were used to characterize the embankment strength distribution with depth. 10 mm diameter (model scale) CPTs were pushed prior to any shaking and following Shakes 3 and 4. Fig. 4a shows the initial measured cone tip resistances (q_c) for the embankments, with a star indicating the reference depth of 1 atm vertical effective stress. The tip resistance profiles increase with C_u, apart from 4CU, which was prepared at a looser relative density than targeted (as discussed at the end of this section). For the sands with larger C_u values, the tip resistances could be elevated due to particle-probe effects as the D_{85} of the soil approaches the diameter of the cone (D_{CPT}). Sturm (2019) found that at D_{CPT}/D_{85} values less than 5, the failure mechanism is compromised, and developed a methodology to correct the elevated profiles to an uncompromised value ($q_{c,Corrected}$) according to equation 1:

$$q_{c,Corrected} = \frac{1}{1.67e^{-0.55(D_{CPT}/D_{85})}+1} \cdot q_c \quad (1)$$

This methodology was applied to these results and the $q_{c,Corrected}$ profiles are shown in Fig. 4b, yet the cone tip profiles did not collapse to the same value, as would be the case if the particle size

were the only source of differences. There remains a clear distinction between profiles due to changes in mechanical properties (e.g., G, e_{max}, e_{min}) of the sands as C_u increases (Sturm 2019). Correlations between q_c and D_r were also developed for the sands included in this study, resulting in equation 2 (Sturm 2019):

$$D_R = 0.75\left(\frac{q_{c1}}{P_a Q}\right)^{0.2} - 1.29 \quad (2)$$

where P_a is 101 kPa, Q is a fitting parameter calculated as:,

$$Q = Q_{FM} Q_{MP} \quad (3)$$

where Q_{MP} was back-calculated by Sturm (2019) and Q_{FM} is calculated as:

$$Q_{FM} = 1.67e^{-0.55(D_{CPT}/D_{85})} + 1 \quad (4)$$

and q_{c1} is calculated as:

$$q_{c1} = \left(\frac{P_a}{\sigma_v'}\right)^{m_e} q_c \quad (5)$$

where m_e = 1 according to centrifuge-specific values computed from literature (Sturm 2019). The Q values are provided in Table 5. Estimations of D_r profiles with depth are shown in Fig. 4c. Beyond a depth of 5 m, where the cone is sufficiently embedded and should not experience shallow-penetration effects, the relative densities are nearly constant with depth. All profiles except for 4CU are effectively built to the same relative density, but this shows that 4CU is approximately 15-20% looser. Upon further maximum density testing following the experiment, the maximum density of 4CU was found to be 1,881 kg/m^3 instead of the reported 1,857 kg/m^3, resulting in an estimated build relative density of 31% instead of the targeted 40%. Since the 4CU model was built looser than the other models, it will not be used directly when discussing trends as a function of C_u; however, it will be included as a reference point to inform parts of the discussion.

4 RESULTS AND DISCUSSION

4.1 DISPLACEMENTS

As the C_u of the test sands increased the horizonal displacements decreased. Fig. 5 shows permanent horizontal displacement contours projected on an embankment outline for shaking events 1-3 for all sands obtained from GEOPIV-RG. The general displacement patterns are consistent with the expected shape for a rotational slope failure in a homogenous material (Varnes 1978). For each shaking event, as C_u increases (i.e., proceeding downward along the columns of embankment outlines), cumulative horizontal displacements diminish. Further, the most broadly graded sand, 12CU, did not experience significant displacements until the third shaking event when the demand on the system was much greater.

Permanent horizontal and vertical displacements increased proportional to the Arias intensity of each shake. Fig. 6 shows the permanent horizontal displacements (ΔX) and vertical displacements (ΔY) accumulated versus I_a of the shaking event, for PIV patches located near the surface of the model in the upslope (a) and midslope (b) array locations – a schematic of the model is included to provide a more precise location of the selected patches marked by stars. I_a is a proxy for energy input into the system. In the upslope patch, 2CU and 4CU incurred appreciable displacements at an I_a of about 0.5 m/s, where 8CU and 12CU did not displace until somewhere between 1.2 to 4 m/s. In the midslope array, the trends are similar, with the only difference in loading being an additional downslope static shear force acting on the soil elements. This increases the demand on the system, leading to displacements at lower I_a across all the sands.

Increasing C_u led to reduced settlements and increased dilatancy of the sands in each shaking event. In the upslope sensor patch in Fig. 6 the vertical settlements decreased with increasing C_u. These settlements appear to be controlled by the down slope movement of the

embankment as they are proportional to the horizontal displacements. However, in the midslope patch, the broadly graded sands did not experience additional settlements with greater horizontal displacements, but instead dilated so strongly during shaking that 12CU heaved above its initial height. This reiterates that even though the soils are at the same D_r, the broadly graded sands dilate more than the poorly graded sands (Kuei 2019, Sturm 2019, Ahmed et al. 2022). This stronger dilatancy is due to the efficient particle packing realized in more broadly graded sands. It is interesting to note that while 4CU is prepared at a looser state and horizontally displaces similarly to 2CU, it settles less as it possibly engages slightly more dilation in the midslope than the 2CU sand. The increase in dilatancy with C_u is a fundamental source for the observed increase in capacity and reduced settlements and horizontal displacements of the broadly graded sands.

These observations of reduced horizontal and vertical settlements per shake and cumulatively may be attributed to how soil behavior changes as the gradation becomes broader. The void ratio corresponding to D_r = 40% reduces from 0.76 to 0.38 for 2CU to 12CU. This results in tighter packing efficiency and particle interlocking, which requires greater dilation for shear straining to occur (Kuei 2019). The resistance to shearing correspondingly increases with the required dilation, resulting in the 12CU generating the shear resistance at smaller strains than a more poorly graded soil like 2CU.

4.2 SPECTRAL ACCELERATION RESPONSE

As C_u increased, the spectral accelerations throughout the depth of the model were more strongly amplified relative to the input motion. The horizontal acceleration time histories were processed to obtain their spectral accelerations (Sa). Fig. 7a shows the Sa response of the surface sensors in the upslope level-ground array (AH6) versus period for all the sands for shakes 1-3. Amplification is defined here as having greater Sa than the base motion, whereas attenuation is a

smaller Sa than the base motion. The Sa responses indicate that an increase in C_u leads to amplification near the predominant period of the input motion, which is 1 second(s). This is more evident in terms of the amplification ratio (Sa at the surface normalized by base Sa), which is shown in Fig. 7b. A ratio below the line represents attenuation while amplification occurs above the line. Around the period of the input motion, 1 second, 2CU and 4CU are attenuated for all shaking events, whereas 8CU is amplified for most shakes, and 12CU is amplified for all shaking events at all periods.

Additionally, a shift in the predominant period of the motion measured by the surface accelerometer indicates that the broadly graded sands better maintained system stiffness (i.e., did not soften). If the response was largely 1D, the initial fundamental period of the sliding mass (T_s) would be calculated as such: $T_s = 4H/V_s$, where H is the height of the sliding mass and V_s is the shear wave velocity of the soil (Bray 2007). Since the height of the embankments remain the same between soils, T_s and V_s are inversely proportional. In Fig. 7a, the predominant period of the Sa for the surface sensor decreases, approaching that of the base motion with increasing C_u, consistent with the shear stiffness increasing with C_u. As shaking intensity increases, the predominant period of all the embankments shifted to longer periods, indicating softening from liquefaction. However, there is a clear trend that the magnitude of softening decreases with increasing C_u, with diminishing returns at high-C_u values, as the broadly graded sands maintain system stiffness.

These trends hold true throughout the depth of the embankment as well. Fig. 7c shows plots of each sensor's Sa ratio at the predominant period of the sensor versus the corresponding period at that peak Sa. The surface sensor is outlined in black, and there is an arrow indicating the progression from the sensor locations at the base of the model to the surface. For each of the embankments, the predominant period lengthens progressing to the surface, as the height of the

soil column underlain increases and the sensors enter soil impacted by liquefaction. The amplification or attenuation response also magnifies progressing from the base to the surface, which must be true to maintain continuity. A visual inspection of the figure reveals that with increasing C_u, vectors rotate counterclockwise, pivoting around the base point and appear to become shorter. A counterclockwise rotation signals increased amplification while a shorter vector reduces the period, indicating a stiffer embankment as discussed previously. While all embankments reached an $r_u = 1$, the broadly graded embankments were stiffer initially, resisted non-linear deformations, and experienced transient stiffnesses from dilation that collectively resulted in greater amplification and better maintained system stiffness.

4.3 EXCESS PORE PRESSURE RESPONSE

The excess porewater pressure response reveals a slight increase in resistance to liquefaction triggering ($r_u = 1$) with increasing C_u. Fig. 8 shows the excess porewater pressure time histories for the two surface pore pressure transducers in the upslope and midslope arrays for all sands. Green markers are included above to indicate the different segments of the applied motion. As C_u increased, the time to liquefaction in P5 increased slightly from just before the constant amplitude cycles (second green line) to immediately following it. In P9, the difference in time to liquefaction is slightly greater. While there are systematic differences in times to liquefaction triggering, indicating an increasing resistance to liquefaction with increasing C_u, the differences are only 2 to 3 seconds, which is relatively small.

The increased dilatancy with C_u results in rapid drops in excess pore pressure that arrest movement. De-liquefaction (Kutter and Wilson 1999) characteristics were noted in 2CU and 8CU soils by Carey et al. (2022a and 2022b) and were equally evident in the 4CU and 12CU soils, as seen in Fig. 8. In the broadly graded sands, these spikes occur twice as often, occurring while

shearing downslope and upslope, and they increase in intensity with increasing C_u (Carey et al. 2022a). The observed dilation spikes in the broadly graded sands reduced the accumulation of displacements.

The excess pore water pressure response indicates that as C_u increased, excess pore pressures dissipate faster. The rate of dissipation is assessed as the duration above an r_u value of 0.5. $r_u > 0.5$ was selected as a value above which straining was most likely to occur. Since liquefaction triggering across the embankments is similar, the duration is reflective of the rate of dissipation of Δu during post-triggering decay of amplitude and post-shaking reconsolidation. Fig. 9 shows the time between the first and last exceedance of $r_u = 0.5$ versus I_a for all the sands for the pore pressure transducers nearest to the surface in the upslope and midslope arrays. In Fig. 9 for the upslope P5 the duration of exceedance decreased significantly as C_u increased. This difference cannot be attributed to permeability, as all soils have very similar permeabilities by design. The faster dissipation in the more broadly graded sands is instead attributed to a stiffer soil matrix (Ahmed et al., 2022) and a lower void ratio, which reduces the volume of water that must be expelled during post-triggering decay of the shaking motion (from possible partial drainage) and post-shaking reconsolidation. The 4CU sand is consistent with this trend of increasing C_u, despite being prepared to a looser relative density (which yet corresponds to a lower void ratio than 2CU). Ultimately, the reduction in time of exceeding an $r_u = 0.5$ led to a faster reestablishment of effective stress, resulting in shear stresses that arrested movement, thus reducing the accumulated deformations.

The behavior at the midslope shown in Fig. 9 exhibits similar trends, though the response of 2CU and 4CU are similar and the response of 8CU and 12CU are similar. The static shear stress present in the slope causes a rapid reduction in Δu as shaking amplitude decayed. Following this

at around 22 s in Fig. 8, the 2CU and 4CU sands began gradually increasing Δu again, whereas the 8CU and 12CU sands continued to dissipate Δu in time. A possible cause for the delayed increase in Δu for 2CU and 4CU after shaking had ceased could be from upward seepage from the underlying soils during reconsolidation. This is supported by the fact that the poorly graded sands experienced more reconsolidation settlements than the more broadly graded sands (as observed by PIV and through volumetric strain estimates in Section 5).

4.4 STRAIN RESPONSE FOR SHAKE 3

Further insights can be gained by examining how strains accumulate in the model. For the sake of brevity, the rest of the discussion will focus on shake 3 (PGA = 0.23 g, I_a = 1.34 m/s) where all embankments sustained high excess pore pressures and deformed significantly. Additionally, only the poorly graded 2CU and most broadly graded 12CU soils will be compared to represent the two behavioral extremes and elucidate the fundamental differences of these materials.

The strains presented herein are derived from the GEOPIV-RG displacement data. Assuming a small element of soil, shear strains (γ) are calculated as the ratio of relative horizontal displacement to initial height of the soil element. Volumetric strains (ε_v) are calculated as the ratio of the change in volume to the original volume, with the implicit assumption that the deformation observed at the boundary exists across the model cross section (Love et al. 2022). This was estimated as the ratio of vertical displacement to the initial height of the soil element. Strains were calculated between GEOPIV-RG patches tracked in time along the entire embankment height.

To improve the strain estimations, displacement data was fit with a third-order polynomial and a geometric correction was applied to the vertical displacement when calculating strain. To obtain a continuous function, each time step of displacement was fit with a third-order equation. The third order was selected as it fit the observed trends and higher-order equations were not

necessary because the models did not have identifiable localized shear planes. Strains were then calculated arithmetically as the first derivative with respect to height of the displacement data curve fits. Additionally, vertical displacements can produce geometric non-linearities, either from rotation or sliding failure, with no local volumetric change. Since the embankments were observed to fail by rotation, a rotation-induced vertical displacement correction was applied when calculating ε_v by subtracting the expected change in y-location from the observed change in y-location. The expected change in y was calculated as the following:

$$\Delta y_{expected} = L - \sqrt{L^2 - \Delta x^2} \quad (6)$$

where L is the length of the element (or initial distance between patches), and Δx is the observed x-displacement. This correction was most important in Shakes 3 and 4 where the embankments experienced significant displacements.

4.4.1 Strain time histories

Focusing on one PIV patch location in the embankment, the shear strain time histories highlight the differences in dynamic strain accumulation, with the broadly graded 12CU strongly resisting accumulation. Fig. 10a presents the shear time histories for the upslope locations for a PIV patch located 2.5 m deep in the model. The shear strain time history for the 2CU embankment begins to steadily accumulate strain soon after shaking begins at 2 s and has an irregular cyclical pattern that is biased to positive strain accumulation. In contrast, the 12CU embankment is largely symmetric about the x-axis until about 8 s, roughly 3 s after $r_u = 1$. In theory, if shaking were to have stopped near when 12CU last crossed the zero-strain line (~8 s), 12CU could have experienced zero permanent strain despite liquefying, where 2CU would have accumulated close to 4% shear strain. Beyond 8 s for 12CU, the amplitude of cyclical shear strains begins to decrease but the cyclic motion is still evident, and it begins to accumulate permanent strains. Further, strains

stop accumulating 5 s sooner, around 15 s when the base motion amplitude is around 0.05 g, while the 2CU embankment does not stop accumulating strains until closer to 20 s when the base motion has essentially ceased. Evidently, the broadly graded embankments resist the initiation of shear strain accumulation and halt movement at higher accelerations and sooner due to the faster dissipation of excess pore pressures.

The volumetric strain time history underscores the strong dilatancy of the broadly graded sands. Fig. 10b shows the volumetric time histories, where negative strain is contraction (settlement) and positive is dilation (heaving). There is notably more scatter in the measurement as the vertical displacements are smaller than the horizontal and come closer to the magnitude of error in GEOPIV-RG. Despite this, it shows that 2CU experienced gradual settlement with instances of rapid settlement (e.g., for 2CU upslope, immediately after 10 s) until it ceased around 15 s. These rapid accumulations of settlement coincide with a slight reversal toward negative shear strain due to loading upslope. Relating this to a stress-strain loop, it is after reversal that the shear stresses drop close to zero, allowing for particle rearrangement and the rapid accumulation of volumetric strains. 12CU shows the opposite response with more gradual accumulation of dilative strains and no clear surges of dilation.

4.4.2 Shear strain accumulation

Throughout the embankment, the broadly graded sands experienced less total shear strain and did not accumulate permanent shear strains until later in the shaking event, despite high excess pore pressures. Fig. 11 compares embankment contours of shear strain in 2CU and 12CU at three instances: start of constant amplitude (when all embankments had reached $r_u \cong 1$), start of decaying amplitude (5 cycles later), and the end of the GEOPIV-RG record (at approximately 19 s). At the end of the record, 12CU experienced less shear strains, with a max strain of 7.0% (displacement =

0.23 m), whereas the 2CU experienced 10.9% (displacement = 0.62 m). Additionally, note that these maximums occurred at different locations in the models and have different contour characteristics. The broadly graded 12CU shows a progressive response with depth with its maximum at the surface in the slope, while the 2CU embankment has a concentration of strains deeper in the model with smaller strains at shallow depth.

4.4.3 Volumetric strain during reconsolidation

Reconsolidation strain estimates from the pore pressure time histories are inversely related to C_u. With dense arrays of pore pressure transducers and assuming 1D flow up a soil column, reconsolidation strains were estimated for each embankment using the method developed by Malvick et al. (2006), which uses Darcy's law to model the flow into and out of virtual soil elements. Excess pore water pressure isochrones were fit for each time step, constraining the excess pore water pressure to zero at the surface and the hydraulic gradient to zero at the base to give no flow at the impermeable boundary. With the fits, the volumetric reconsolidation strains were estimated. Fig. 12 shows estimates of reconsolidation strain for the upslope array, which best approximates the 1D flow behavior that the method was developed for. The estimated strain is approximately 2% and 1% reconsolidation strains in the 2CU and 12CU embankments, respectively, which are consistent with the average volumetric strains of 2.2% and 0.7% measured by GEOPIV-RG. The differences in strains indicate that the volume of water expelled in 12CU was about half that of 2CU. This further strengthens the attribution of the rapid dissipation of excess pore pressure of the more broadly graded sands to the lower void ratio and higher bulk modulus. The midslope estimations (not shown here) did not agree with measurements by GEOPIV-RG as the shear-induced dilation offset some of the reconsolidation components.

4.4.4 Strain rates

Strain rates, derived from the time histories, highlight differences in the accumulation of shear strain. This is exemplified using a single cycle in the motion, from approximately 9.5 to 10.5 s in Fig. 10, with the time of interest in Fig. 13 showing the strain rates versus time. In Fig. 10, at the peaks and valleys of strain, motion stops and direction is reversed (i.e., zero strain rate in Fig. 13). The midpoints between peaks are when strain accumulation is the fastest (i.e., maximum strain rate in Fig. 13). Conceptually this corresponds to the points on a stress-strain loop near zero stress at the base of the loop where strain accumulates rapidly. Comparing the two shear strain rates for the upslope array, the 12CU embankment has much narrower and stronger peaks in strain rate than 2CU, which are broader and weaker. It is also notable that for 2CU, there is not the reversal to negative strain rate that is seen in 12CU, but it is replaced by a positive down-slope peak in strain, albeit smaller than the other peaks. Similarly, for the volumetric strain rates, the 2CU stays in the negative contraction region and does not strongly dilate. The 12CU volumetric strain behavior conversely has consistent and regular peaks in both dilation and compression. Interestingly, in both embankments, there is an apparent phase lag between zero shear strain rate and dilation peaks that was not expected. The authors expected to see a peak in dilation when the shear strain equals zero, but it is not until ~$1/8^{th}$ of a cycle later that the peak occurs. It is possible that this is due to unequalized pore pressures in the model (Kim et al. 2020) or potentially continued expansion from the soil below, which is at a different phase in the shear wave propagation.

With the shear strain rates and pore pressures directly measured, their interdependency was evaluated. Fig. 14 demonstrates schematically how shear strain rate and r_u are expected to depend on one another. At high r_u values, the effective stress is reduced and the strain rate increases exponentially, and vice versa. Thus, a dilation spike would rapidly drop excess pore pressures to

zero, simultaneously reducing the strain rate to zero. Fig. 15 is a compilation of all the strain rates for each pore pressure transducer at 1/4 cycles, versus the corresponding excess pore water pressure ratio values. The broader trends align with the expected behavior, with high strains at high pore pressures and vice-versa. In the upslope level ground condition, it appears that the strain rate begins increasing at an $r_u > 0.4$ whereas in the midslope it is closer to $r_u > 0.6$. These trends further support that the dilation spikes, which decreased r_u to less than zero, decreased the strain rate to zero, thus reducing the accumulation of strains.

4.5 SUMMARY OF TRENDS AS FUNCTION OF CPT

There is a strong link between the initial CPT cone tip resistance and the accumulated deformations for the range of test conditions evaluated. CPT cone tip resistances depend on the embankment's relative density, state, void ratio, and gradation. Similarly, the displacements accumulated in shaking are also dependent on these parameters. Thus, the q_{c1} and observed displacements are expected to be related in an inverse manner. Fig. 16 shows the total accumulated displacements measured by PIV after shakes 1, 3, and 4 for a patch near the surface of the model aligned with accelerometer AH11 in the midslope array, compared with the initial cone tip resistance at 1 atm in the model. Data points were included from a previous test on 2CU and 8CU at $D_r = 63\%$ (Carey et al. 2022a and Carey et al. 2022b) to increase the range of cone tip resistances observed. There is a clear relationship between cone tip resistances and displacement accumulation for the set of conditions varied in these centrifuge tests, but additional research is necessary to expand the observed trends into a framework that is more broadly applicable.

5 CONCLUSIONS

The results of this test series address some fundamental assumptions in liquefaction engineering and design. Although all the embankments experienced liquefaction triggering ($r_u =$

1) and sustained elevated excess pore pressures, the associated consequences of liquefaction were reduced as soil gradation broadened, despite being prepared to the same relative density.

The sands used in these experiments captured the range of expected void ratios, while the void ratio and CPT cone tip resistance highlight differences due to gradation. The void ratio extrema of the sands used in these experiments align with the average values from the broader set of data, so the trends observed may be more broadly useful. The soils tested span over 80% of the range of extrema, thus minimal further reductions in deformations are expected at gradations broader than 12CU. Finally, the cone tip resistances of these sands were distinct and increased with C_u, despite being prepared to the same relative density and correcting for particle-to-probe effects. However, there is an apparent correlation between initial embankment cone tip resistances and ultimate accumulation of deformations that should be explored further.

Broadening soil gradation causes fundamental changes in multiple index and density metrics, which lead to distinct system level responses clearly evident in the displacements and strain behavior, acceleration response, and pore water pressure time histories. An increase in C_u led to changes in index and density metrics, affecting the material behavior when loaded, and ultimately changing the observed system-level response. C_u is also easy to measure compared to in-situ void ratio or density. In summary, an increase in C_u led to:

- reduced horizontal displacements. Lower void ratio and increased particle interlocking leads to increased dilatancy, which leads to higher shear capacity and stronger and more frequent dilation spikes, which drop excess pore pressures and arrest movement, thus initially delaying and then more rapidly arresting the accumulation of strains, which reduces the total permanent horizontal displacements. In terms of C_u, there was a slight reduction (if at the same D_r) from C_u = 2 to 4, significant reduction from 4 to 8, and

slight reduction from 8 to 12, with a reduction in max displacements of 50% from 2 to 12.

- reduced settlements and potentially upward movement. The lower void ratio and greater packing efficiency lead to stronger dilation and a greater bulk modulus, which lead to less particle rearrangement and reconsolidation strains, ultimately reducing settlements, and potentially even resulting in net dilative displacements. In terms of C_u, the progression was relatively linear from C_u = 2 to 12 in the midslope, with C_u = 8 near zero net settlements for these experiments.
- increased amplification across the depth of the model. More efficient packing and lower void ratio lead to increased model stiffness and dilation, which preserves and transmits the motion, resulting in amplification at the surface. From C_u = 2 to 8, the response was approximately 2x more amplified at the surface, while from 2 to 12, the response was nearly 3x more amplified, depending on the applied motion.
- rapid dissipation of excess pore pressures. The lower void ratio and greater bulk modulus reduce the volume of water expelled and retain more load on the soil skeleton, resulting in faster dissipation of excess pore pressure, which reestablish effective stresses, thus arresting movement and ultimately decreasing permanent deformations. In the level ground, the duration of exceedance of r_u = 0.5 appear to decay exponentially with C_u to short durations.

The results of this experiment stress the importance of considering sand gradation in evaluation of liquefaction susceptibility. There is a systematic effect of gradation on the behavior and performance of sands that relative density alone is insufficient to capture, but additional research is required to account for this in the assessment of liquefaction susceptibility. There is a

strong case to use C_u, as it is a single parameter that controls multiple index and density metrics, which produce unique responses.

6 ACKNOWLEDGEMENTS

The National Science Foundation (NSF) provided the funding for this centrifuge experiment by grant number CMMI-1916152 and the Natural Hazards Engineering Research Infrastructure (NHERI) provided funding for the shared use centrifuge facility at University of California at Davis under grant No. CMMI-1520581. The authors would like to acknowledge and thank the following individuals for their assistance during planning and testing: Jakob Strasilla, Dr. Dan Wilson, Tom Kohnke, Chad Justice, and Anatoliy Ganchenko.

7 REFERENCES

Ahmed, S. S., & Martinez, A. (2020). Modeling the mechanical behavior of coarse-grained soil using additive manufactured particle analogs. Acta Geotechnica, 15(10), 2829–2847. https://doi.org/10.1007/s11440-020-01007-6

Ahmed, S.S., Martinez, A., and DeJong, J.T. (n.d.). Effect of Gradation on the Strength and Stress-Dilation Behavior of Coarse-Grained Soils in Drained and Undrained Triaxial Compression.

Been, K., and Jefferies, M.G. 1985. A state parameter for sands. Géotechnique, 35(2): 99–112. ICE Publishing. doi:10.1680/geot.1985.35.2.99.

Bolton, M.D. 1986. The strength and dilatancy of sands. Géotechnique, 36(1): 65–78. doi:10.1680/geot.1986.36.1.65.

Boulanger, R.W. 2003. Relating Kα to Relative State Parameter Index. Journal of Geotechnical and Geoenvironmental Engineering, 129(8): 770–773. American Society of Civil Engineers. doi:10.1061/(ASCE)1090-0241(2003)129:8(770).

Bray, J.D. 2007. Simplified Seismic Slope Displacement Procedures. In Earthquake Geotechnical Engineering. Edited by K.D. Pitilakis. Springer Netherlands, Dordrecht. pp. 327–353.

Carey, T.J., Chiaradonna, A., Love, N.C., Wilson, D.W., Ziotopoulou, K., Martinez, A., and DeJong, J.T. 2022(a). Effect of soil gradation on embankment response during liquefaction: A centrifuge testing program. Soil Dynamics and Earthquake Engineering, 157: 107221. doi:10.1016/j.soildyn.2022.107221.

Carey, T.J., Love, N.C., DeJong, J.T. 2022(b). The liquefaction and cyclic-mobility performance of embankment systems constructed with different sand gradations. [Manuscript in preparation]

Carey, T.J., Love, N.C., DeJong, J.T., Ziotopoulou, K., and Martinez, A. 2022(c). Effect of Soil Gradation on the Response of a Submerged Slope when Subjected to Shaking – Centrifuge Data Report for TJC02. Center for Geotechnical Modeling, University of California, Davis.

Cimini, D. 2016. Investigation of Permeability and Clogging of Ottawa F-65 Sand Saturated with Dow F50 Methylcellulose. University of California, Davis.

Dhakal, R., Cubrinovski, M., and Bray, J.D. 2022. Evaluating the applicability of conventional CPT-based liquefaction assessment procedures to reclaimed gravelly soils. Soil Dynamics and Earthquake Engineering, 155: 107176. doi:10.1016/j.soildyn.2022.107176.

Garnier, J., Gaudin, C., Springman, S.M., Culligan, P.J., Goodings, D., Konig, D., Kutter, B., Phillips, R., Randolph, M.F., and Thorel, L. 2007. Catalogue of scaling laws and similitude questions in geotechnical centrifuge modelling. International Journal of Physical Modelling in Geotechnics, 7(3): 01–23. doi:10.1680/ijpmg.2007.070301.

Idriss, I.M., and Boulanger, R.W. 2008. Soil liquefaction during earthquakes. Earthquake Engineering Research Institute (EERI), Oakland, CA.

Kim, S.-N., Ha, J.-G., Lee, M.-G., & Kim, D.-S. (2020). LEAP-UCD-2017 Centrifuge Test at KAIST. In B. L. Kutter, M. T. Manzari, & M. Zeghal (Eds.), Model Tests and Numerical Simulations of Liquefaction and Lateral Spreading (pp. 315–339). Springer International Publishing. https://doi.org/10.1007/978-3-030-22818-7_16

Konrad, J.-M. 1988. Interpretation of flat plate dilatometer tests in sands in terms of the state parameter. Géotechnique, 38(2): 263–277. ICE Publishing. doi:10.1680/geot.1988.38.2.263.

Kuei, K.C. 2020, Pile Dynamics and Shearing Behavior of Granular Soils, Doctoral dissertation, University of California, Davis.

Kutter, B.L., and Wilson, D.W. (n.d.). De-liquefaction shock waves. In 7th US-Japan Workshop on Earquake Resistant Design of Lifeline Facilities and Countermeasures Against Soil Liquefaction. p. 15.

Love, N.C., Carey, T.J., DeJong, J.T., Wilson, D.W., 2022. Tracking Seismically-induced Embankment Deformations Using High-speed Camera Arrays and PIV in a Large Centrifuge Model. Presented at the 10th International Conference on Physical Modelling in Geotechnics, KAIST, Daejeon, Korea.

Malvick, E.J., Kutter, B.L., and Boulanger, R.W. 2008. Postshaking Shear Strain Localization in a Centrifuge Model of a Saturated Sand Slope. Journal of Geotechnical and Geoenvironmental Engineering, 134(2): 164–174. doi:10.1061/(ASCE)1090-0241(2008)134:2(164).

Pires-Sturm, A.P., and DeJong, J.T. 2022. Influence of Particle Size and Gradation on Liquefaction Potential and Dynamic Response. Journal of Geotechnical and Geoenvironmental Engineering, 148(6): 04022045. doi:10.1061/(ASCE)GT.1943-5606.0002799.

Rollins, K.M., Roy, J., Athanasopoulos-Zekkos, A., Zekkos, D., Amoroso, S., and Cao, Z. 2021. A New Dynamic Cone Penetration Test–Based Procedure for Liquefaction Triggering Assessment of Gravelly Soils. Journal of Geotechnical and Geoenvironmental Engineering, 147(12): 04021141. doi:10.1061/(ASCE)GT.1943-5606.0002686.

Ruttithivaphanich, P., and Sasanakul, I. 2022. Liquefaction Evaluation of a Gravel-Sand Mixture Using Centrifuge Tests. In Geo-Congress 2022. American Society of Civil Engineers, Charlotte, North Carolina. pp. 288–296.

Shepard, G. 2018. Characterization of Coarse Grained Soil Mixes for Investigation of Penetrometer to Particle Size Effects Using Centrifuge Modeling. Thesis, University of California, Davis.

Stanier, S.A., Blaber, J., Take, W.A., and White, D.J. 2016. Improved image-based deformation measurement for geotechnical applications. Canadian Geotechnical Journal, 53(5): 727–739. doi:10.1139/cgj-2015-0253.

Sturm, A.P. 2019. On the liquefaction potential of gravelly soils: Characterization, triggering and performance. Doctoral dissertation, University of California, Davis.

Pires-Sturm, A.P., Jaeger, R., DeJong, J.T., 2022. Estimating Maximum and Minimum Void Ratio from Index Parameters. Presented at the Dam Safety 2022, Association of State Dam Safety Officials, Inc., Baltimore, MD.

Taylor, D.W. 1948. Fundamentals of Soil Mechanics. John Wiley & Sons, Inc.

Varnes, D.J. 1978. Slope movement types and processes.

Wang, T., Liu, S., Wautier, A., and Nicot, F. 2022. Updated skeleton void ratio for gravelly sand mixtures considering effect of grain-size distribution. Canadian Geotechnical Journal, 59(1): 12–23. doi:10.1139/cgj-2020-0570.

TABLES

Table 1. Sand mixture details. US Silica soils.

Commercial name	***Nomenclature (Sturm 2019)***	***D_{50} (mm)***	***Percent by mass (%)***			
			2CU	*4CU*	*8CU*	*12CU*
SILICA SAND #140-200 (#110)	-	*0.09*	-	-	-	*4.8*
SILICA SAND #100-140	-	*0.13*	-	-	-	*4.8*
NJ-#70	*100A*	*0.18*	*100.0*	*33.3*	*25.0*	*4.8*
NJ-#6	*100B*	*0.51*	-	*33.3*	*25.0*	*19.0*
NJ-#1	*100C*	*1.31*	-	*33.3*	*25.0*	*19.0*
NJ-#3	*100D*	*2.58*	-	-	*25.0*	*23.8*
NJ-#1/4	-	*6.35*	-	-	-	*23.8*

Table 2. Soil properties (2CU/100A, 4CU/33ABC, and 8CU/25ABCD reproduced partly from Sturm 2019).

Sand	***USCS***	***D_{10}***	***D_{30}***	***D_{60}***	***Cu***	***Cc***	***e_{min}***	***e_{max}***	***e @ D_r = 40%***	***State parameter (ξ)***	***Relative state parameter (ξ_R)***	***Permeability (k)***
		[mm]	*[mm]*	*[mm]*								*[cm/s]*
2CU	*SP*	*0.12*	*0.15*	*0.20*	*1.7*	*1.02*	*0.579*	*0.881*	*0.760*	*-0.096*	*-0.32*	*0.025*
4CU	*SP*	*0.15*	*0.26*	*0.66*	*4.4*	*0.68*	*0.397*	*0.622*	*0.532*	*-0.084*	*-0.37*	*0.031*
8CU	*SP*	*0.16*	*0.36*	*1.21*	*7.5*	*0.67*	*0.303*	*0.544*	*0.448*	*-0.085*	*-0.35*	*0.026*
12CU	*SW*	*0.18*	*0.66*	*2.20*	*12.4*	*1.11*	*0.276*	*0.450*	*0.380*	*-0.067*	*-0.38*	*0.030*

Table 3. Achieved metrics of the applied motion (PGA and I_a) for shakes 1 to 4.

Shake	***# Cycles***	***PGA***	***I_a***
		[g]	*[m/s]*
1	*7*	*0.14*	*0.32*
2	*8*	*0.17*	*0.58*
3	*20*	*0.23*	*1.34*
4	*20*	*0.40*	*4.42*

Table 4. Shear wave velocity and shear stiffness near an effective stress of 90 kPa (2CU and 8CU from Carey et al. 2022)

	Dr = 63%		***Dr = 40%***	
	2CU	*8CU*	*4CU*	*12CU*
V_s (m/s)	*164*	*199*	*188*	*217*
G_{max} (MPa)	*51*	*84*	*72*	*102*

Table 5. Fitting parameters for all sands (2CU, 4CU, and 8CU reproduced from Sturm 2019). (* assumed to be the same as 8CU since 12CU was not tested by Sturm 2019. True value expected to be greater.)

Sand	Q_{MP}	Q_{FM}	***Q***
2CU	*1.00*	*1.00*	*1.00*
4CU	*0.97*	*1.03*	*1.00*
8CU	*1.36*	*1.17*	*1.60*
12CU	*1.36**	*1.42*	*1.93*

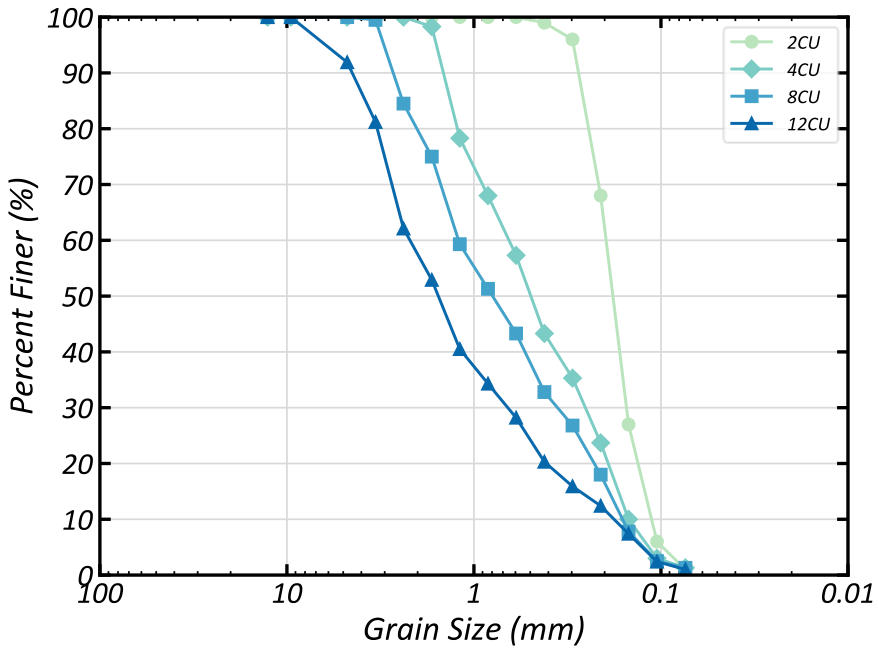

Figure 1. Grain size distribution plot for sands 2CU, 4CU, 8CU, and 12CU.

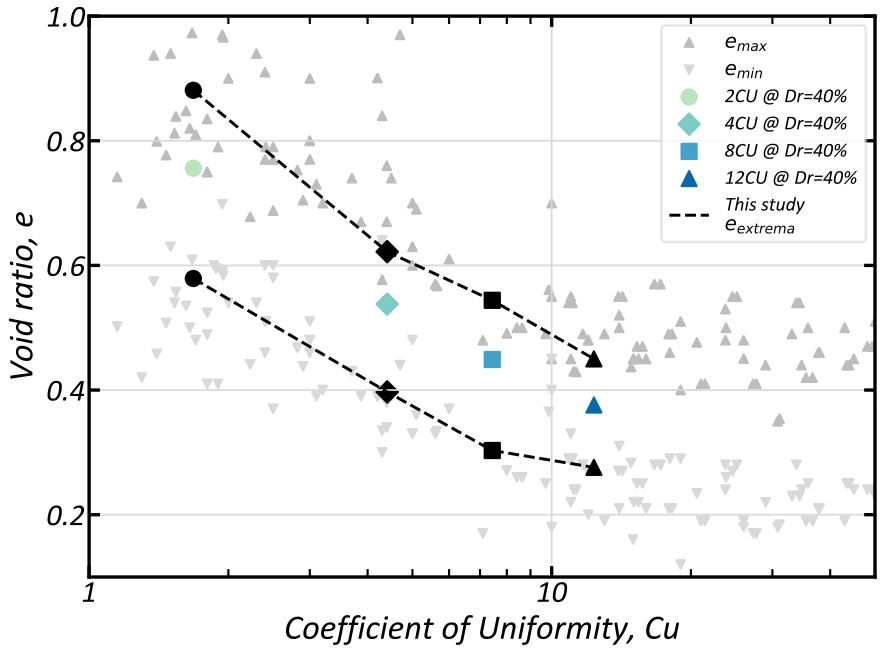

Figure 2. Void ratio extrema for the test soils, along with data points in grey from a broader set of in-situ soils (Sturm and DeJong 2022). The colored points represent the void ratios at the target D_r = 40%.

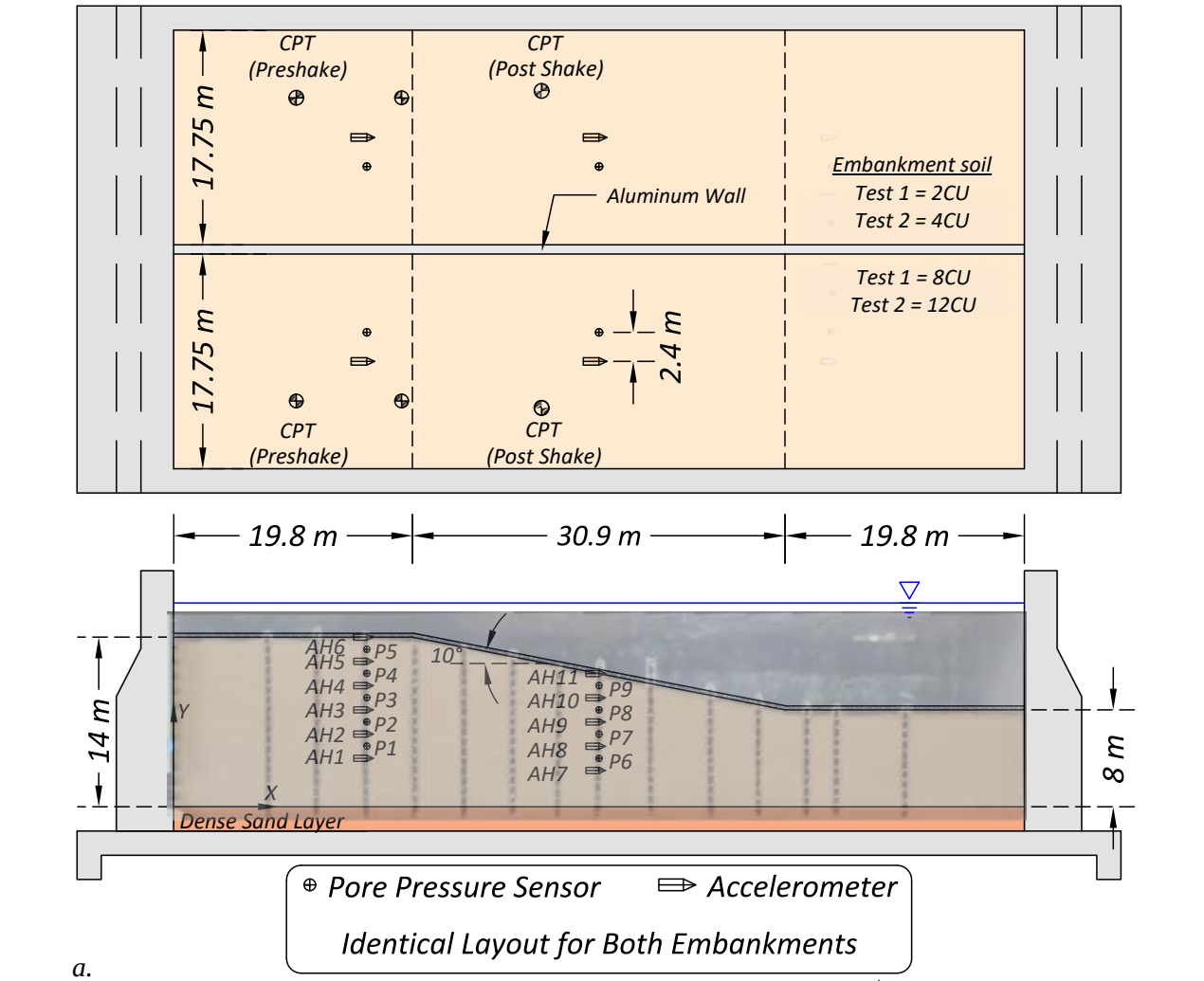

a.

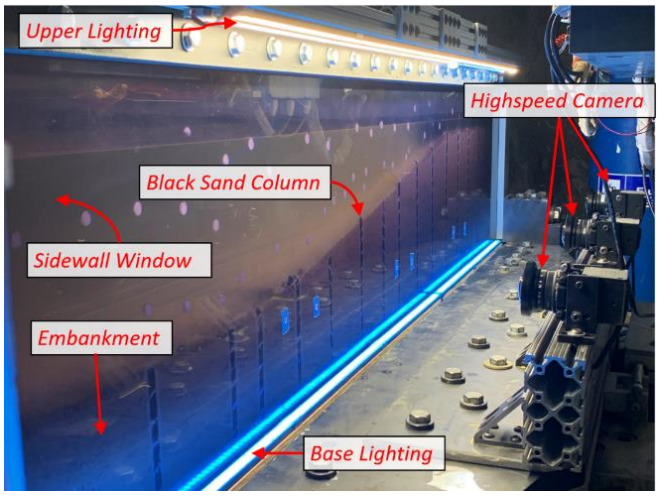

b.

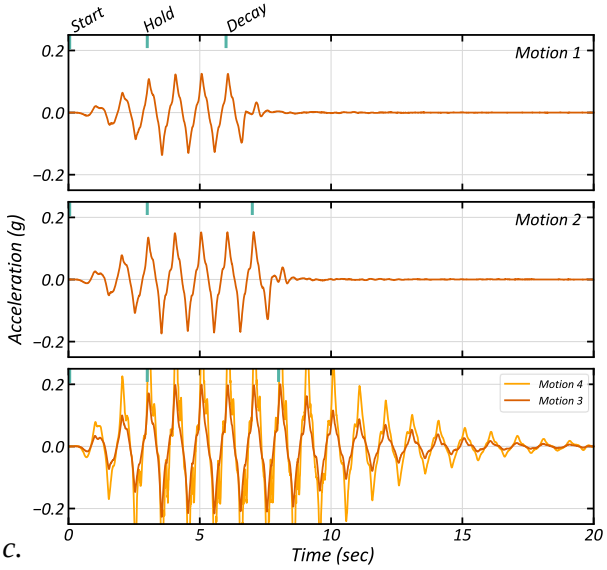

c.

Figure 3. Summary figure of experimental setup including, a. model layout including black sand columns, b. video recording setup, c. motion signatures with motion 4 in grey behind motion 3.

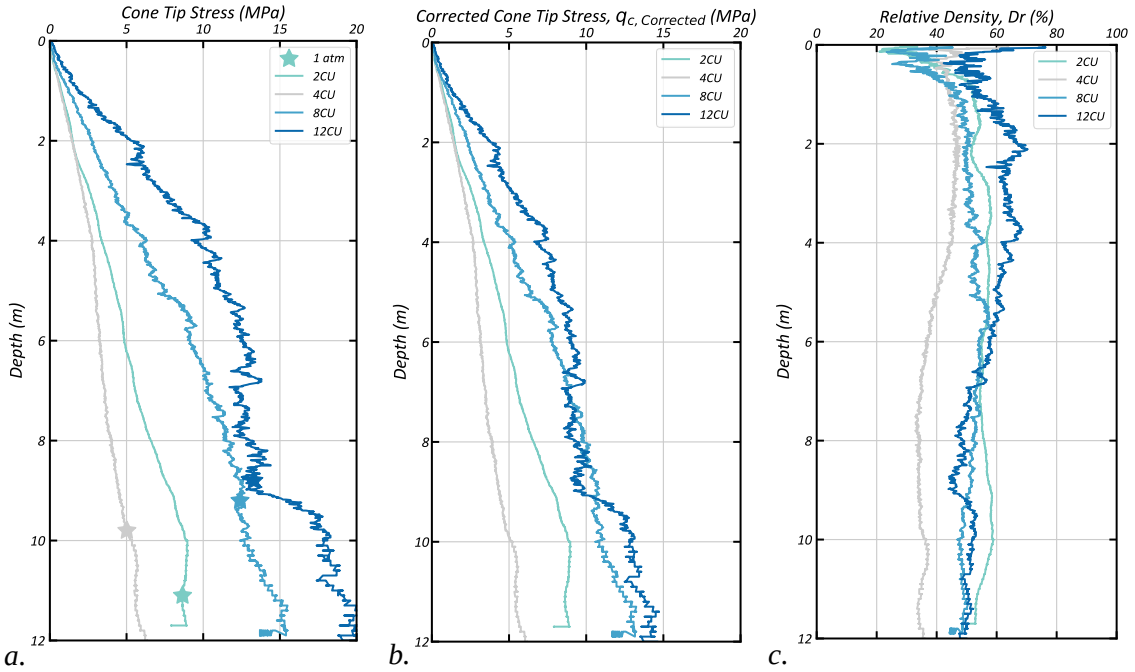

Figure 4. Profiles with depth of, a. cone tip resistance, b. corrected cone tip resistance, and c. relative density estimation with depth using Sturm's (2019) method.

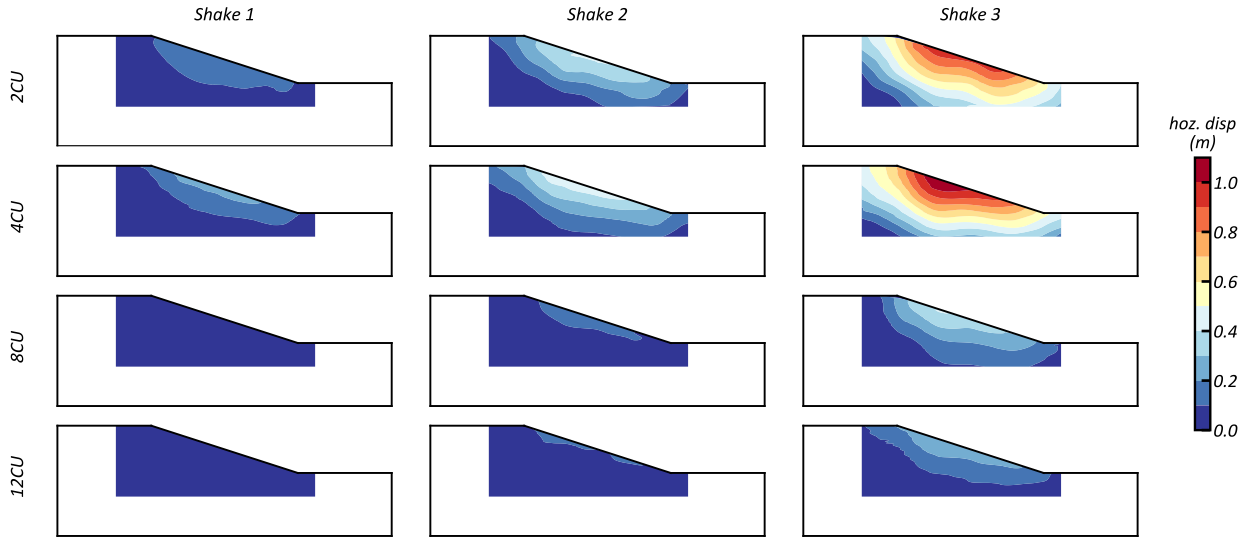

Figure 5. Permanent embankment horizontal displacement contours for shakes 1-3 and all sands. 4CU was erroneously built at a D_r of 31% where the other sands were built close to the target D_r of 40%.

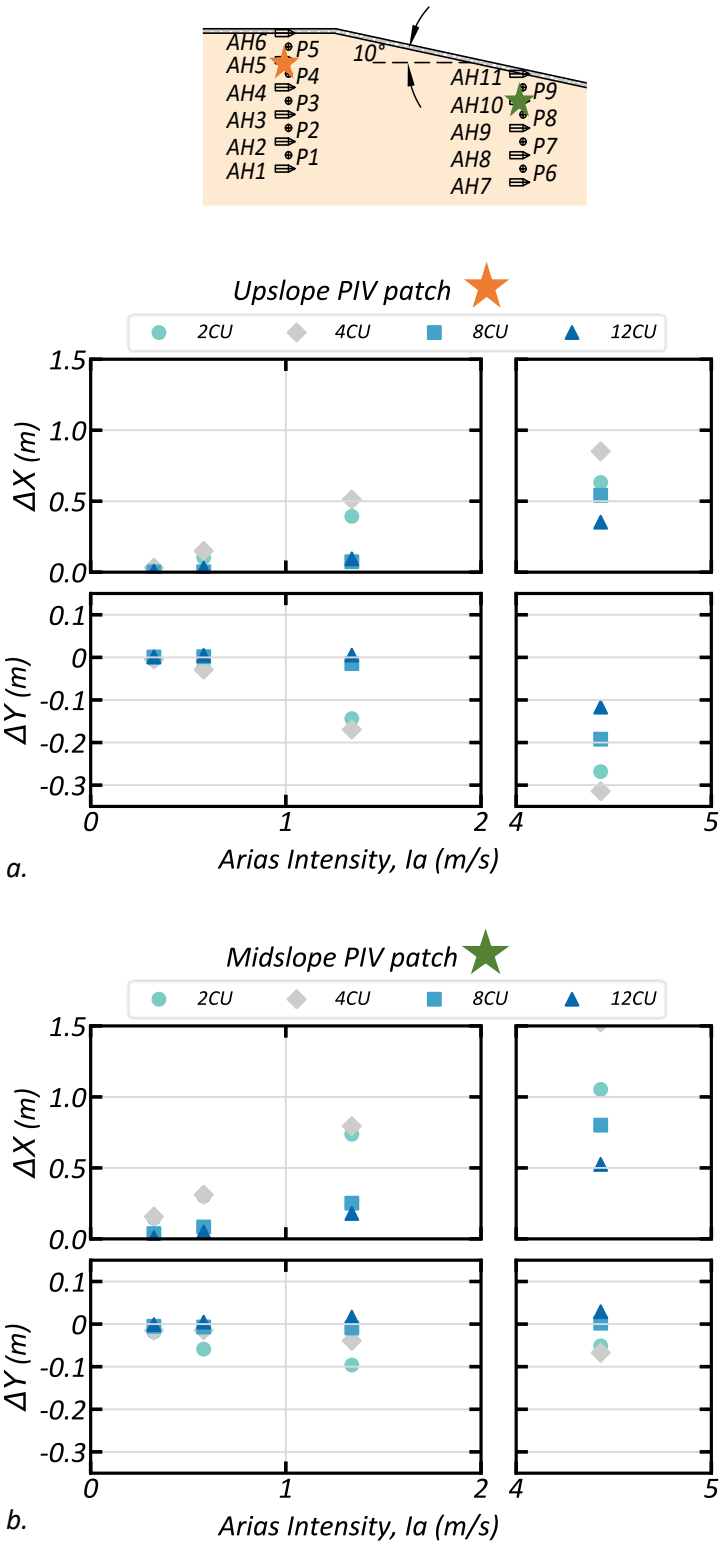

Figure 6. Permanent horizontal and vertical displacements versus Arias intensity for each shaking event for patches near the surface in the upslope (a) and midslope (b) array regions. More precise locations shown in the model snip above the figures.

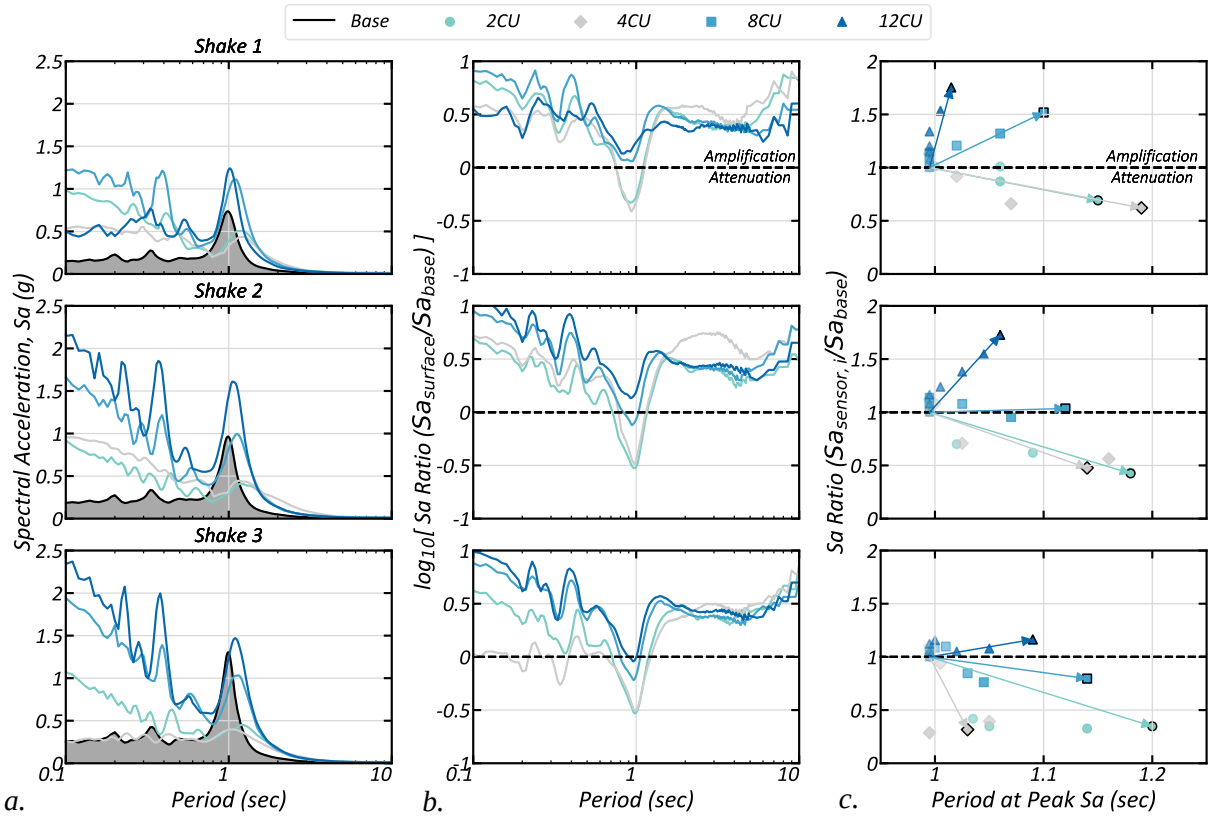

Figure 7. Acceleration time history records from shakes 1-3 for the upslope array, processed to obtain the: a. spectral acceleration (Sa) at for the surface sensor versus period, b. log of the ratio of the Sa of the surface relative to the base versus period to highlight amplification and attenuation, and c. Peak Sa ratio of each sensor in the array relative to the base versus period at the peak Sa, where the black outlined marker indicates the surface accelerometer and the arrow indicates the progression of sensors from the base to the surface.

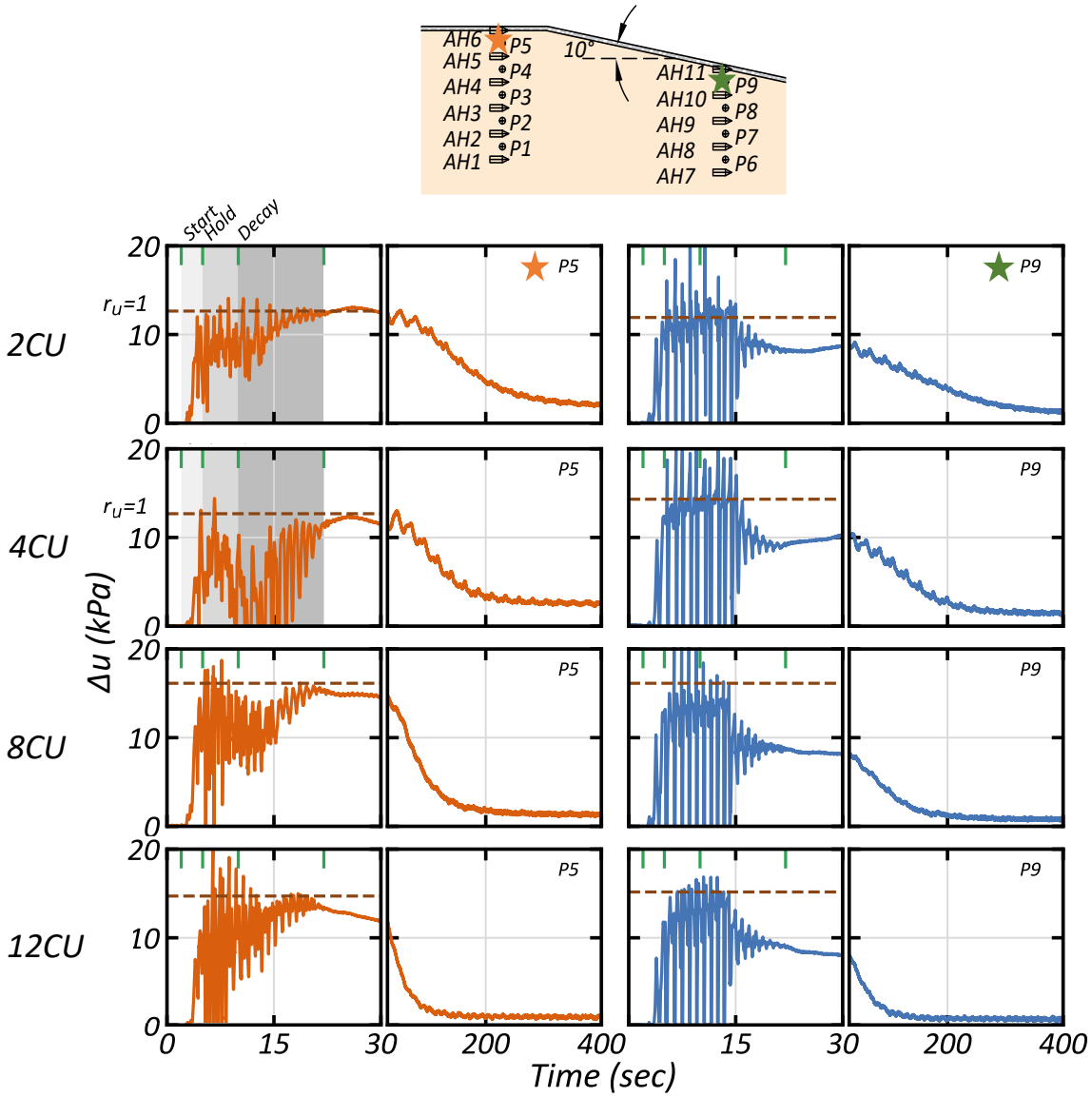

Figure 8. Excess porewater pressure time histories for sensors P5 and P9 for all sands.

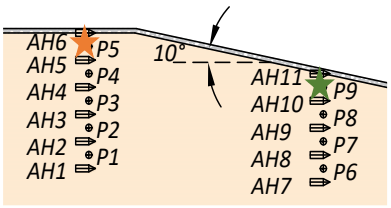

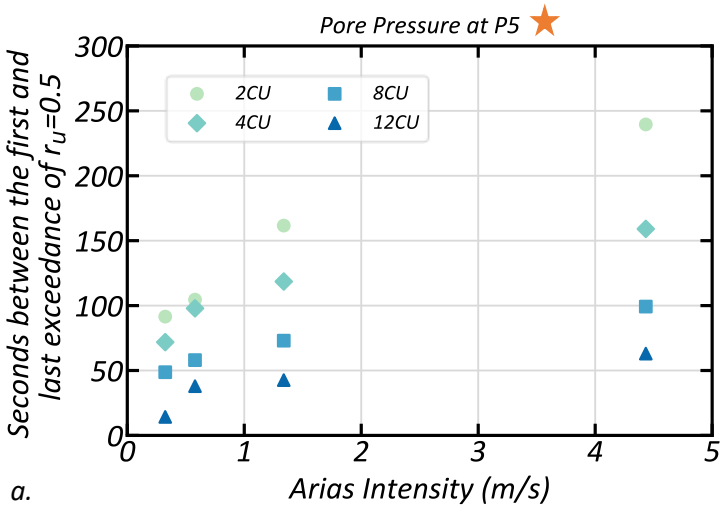

a.

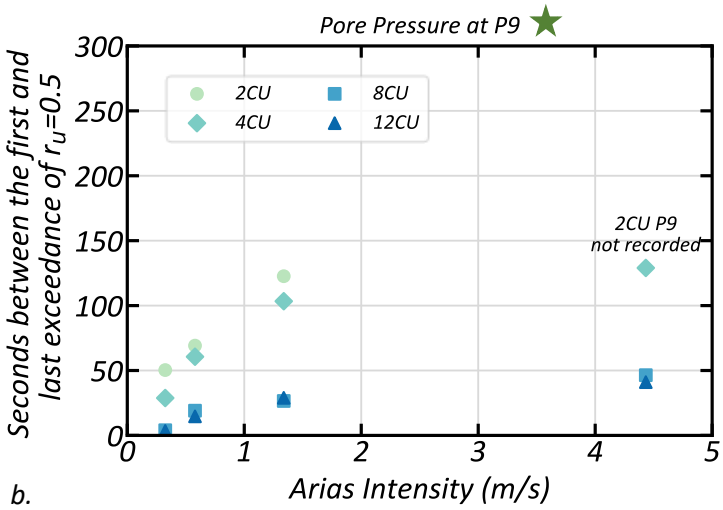

b.

Figure 9. Time between first and last exceedance of r_u=0.5 versus Ia for ppt sensors near the surface: P5 (a) and P9 (b). Location shown in model snip above the figures.

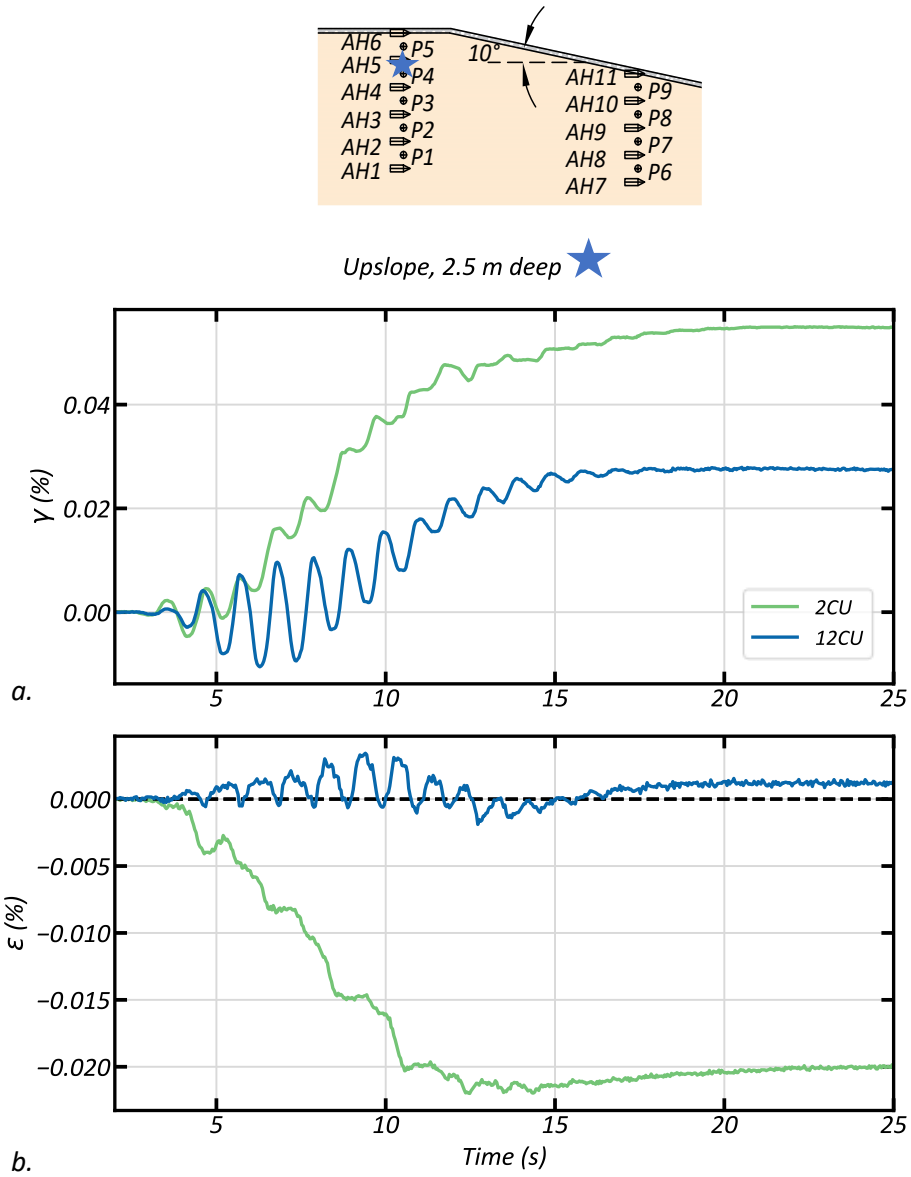

Figure 10. Shear strain (a) and volumetric strain (b) time histories from the fit data for the upslope location, at a depth of 2.5 m. Above the dashed line is dilation, below is compression/settlement.

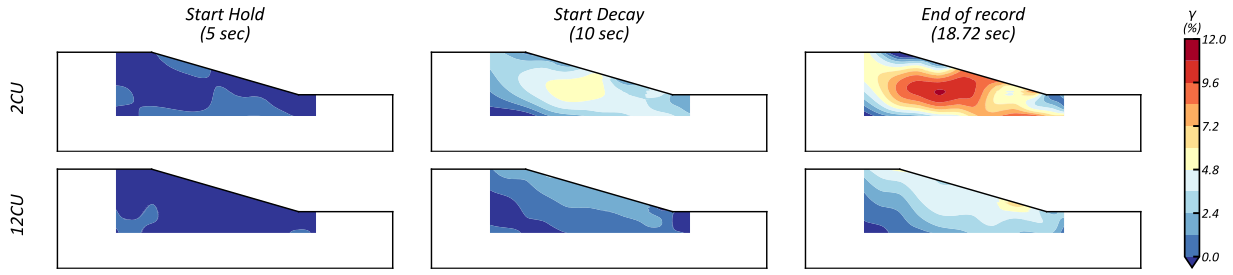

Figure 11. Shear strain contours for 2CU and 12CU for three instances in the motion: start of holding amplitude (5 s), start of decaying amplitude (10 s), and end of processed record (18.7 s).

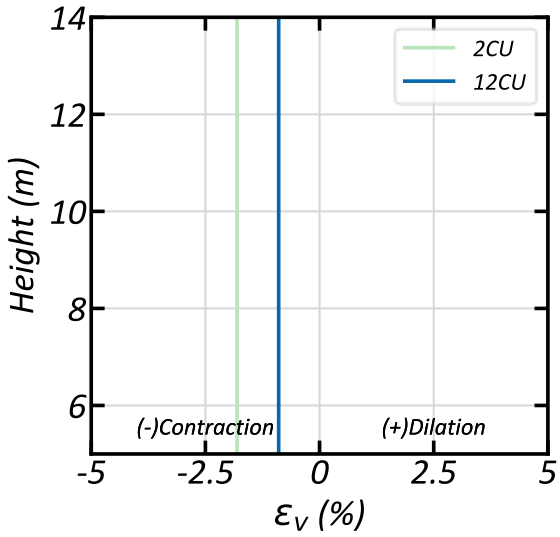

Figure 12. Volumetric reconsolidation strain estimates for the upslope array for 2CU and 12CU.

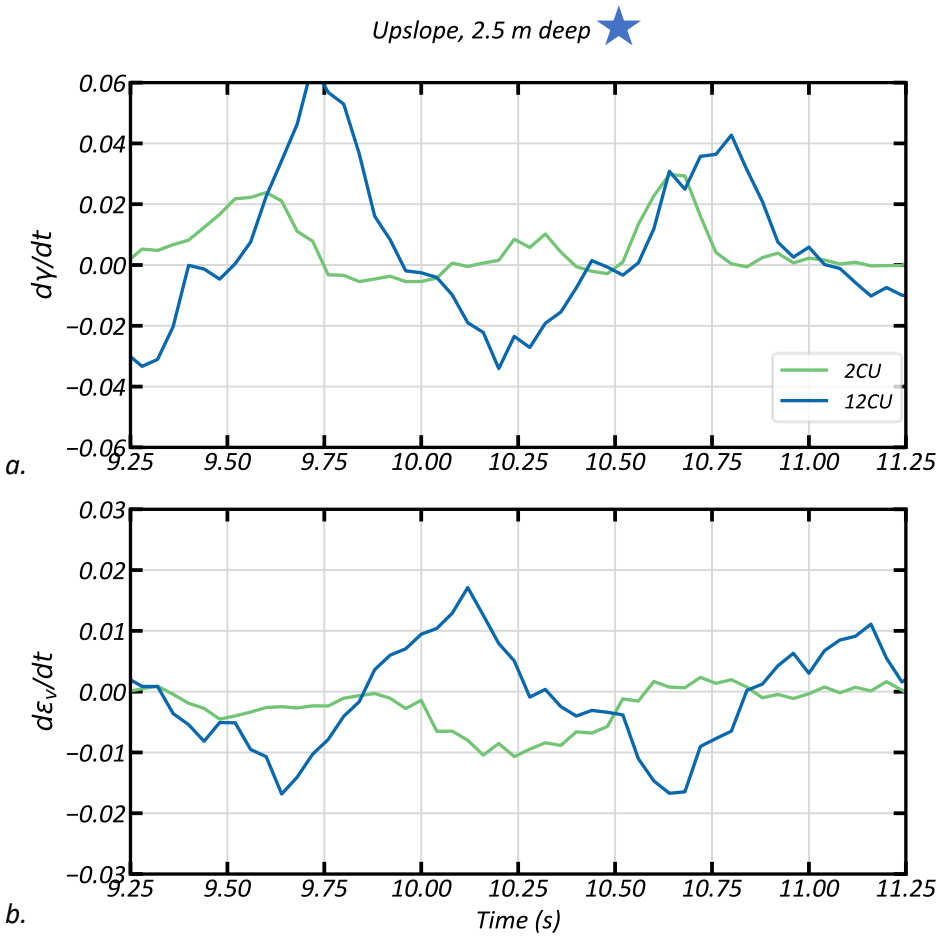

Figure 13. Shear strain rate (a) and volumetric strain rate (b) time histories between 9.25 s and 11.25 s for the upslope location, at a depth of 2.5 m.

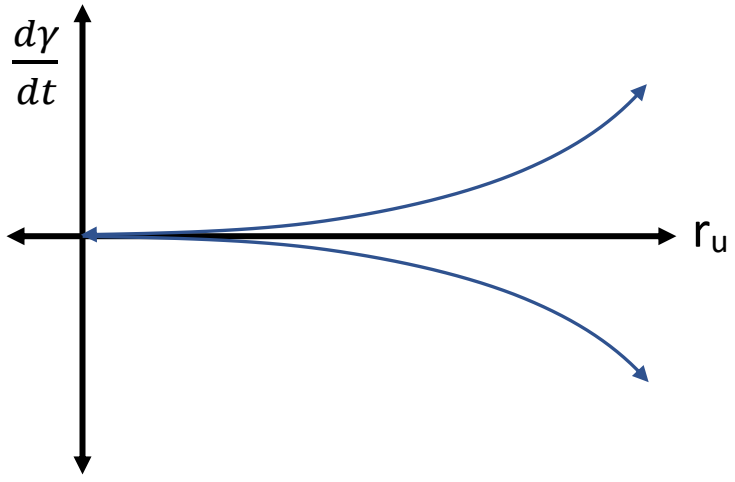

Figure 14. Conceptual plot of the expected trend of strain rate with increasing excess pore water pressure ratio (r_u).

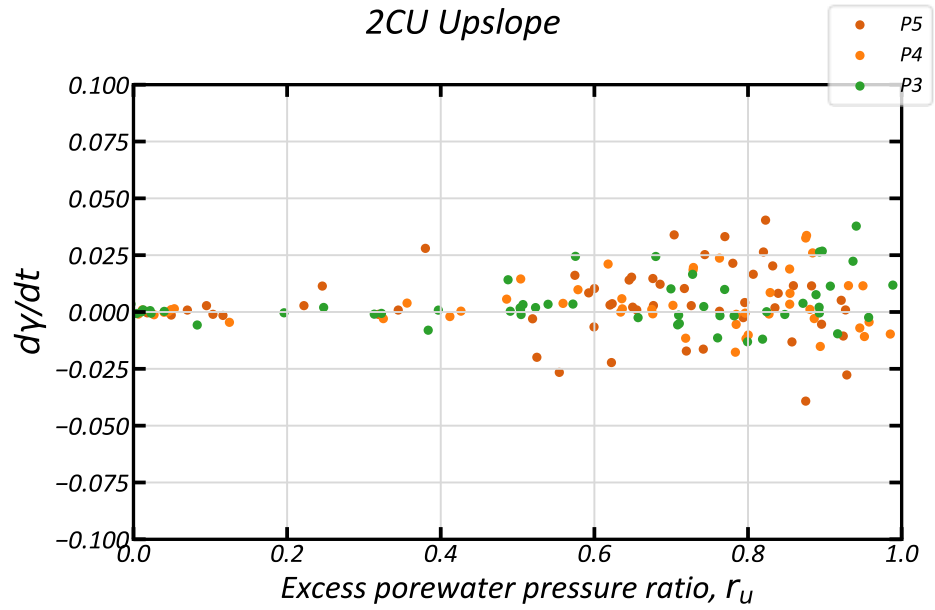

a.

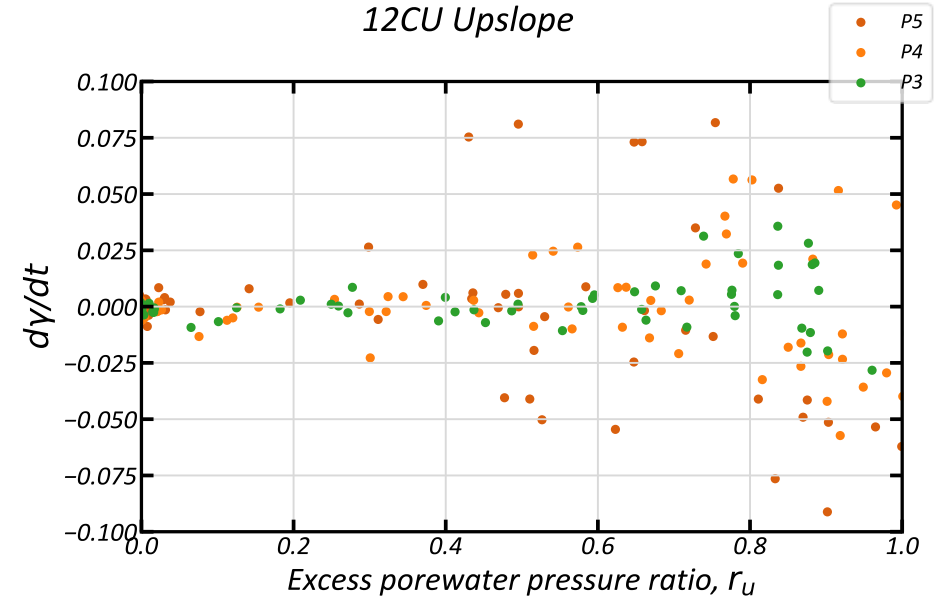

b.

Figure 15. Shear strain rate from PIV data versus excess porewater pressure ratio (r_u) from pore pressure transducer data for 2CU (a) and 12CU (b), including data from three upper sensors from the upslope array, from 2 to 10 s.

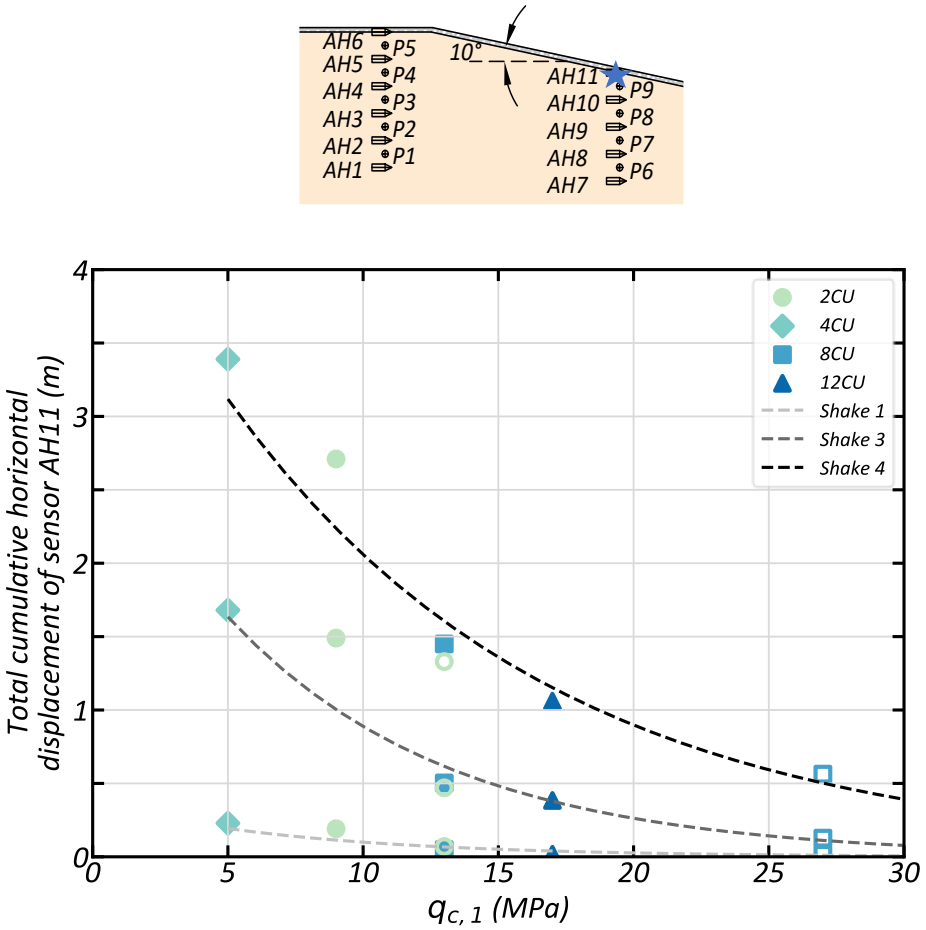

Figure 16. Example trend of cumulated displacements of AH11 with initial cone tip resistances. Closed symbols are for D_r = 40%, while open symbols represent D_r = 63%.

Table S1. Permeabilities at the different relative densities/ void ratios.

Sand	emin	emax	ebuild	k @ Dr = 20%	ebuild	k @ Dr = 40%	ebuild	k @ Dr = 80%
100A	0.58	0.87	0.82	0.027	0.76	0.025	0.64	0.020
33ABC	0.39	0.62	0.57	0.038	0.53	0.030	0.43	0.018
25ABCD	0.31	0.53	0.49	0.043	0.44	0.024	0.35	0.007
12CU	0.28	0.45	0.42	0.056	0.38	0.030	0.31	0.009

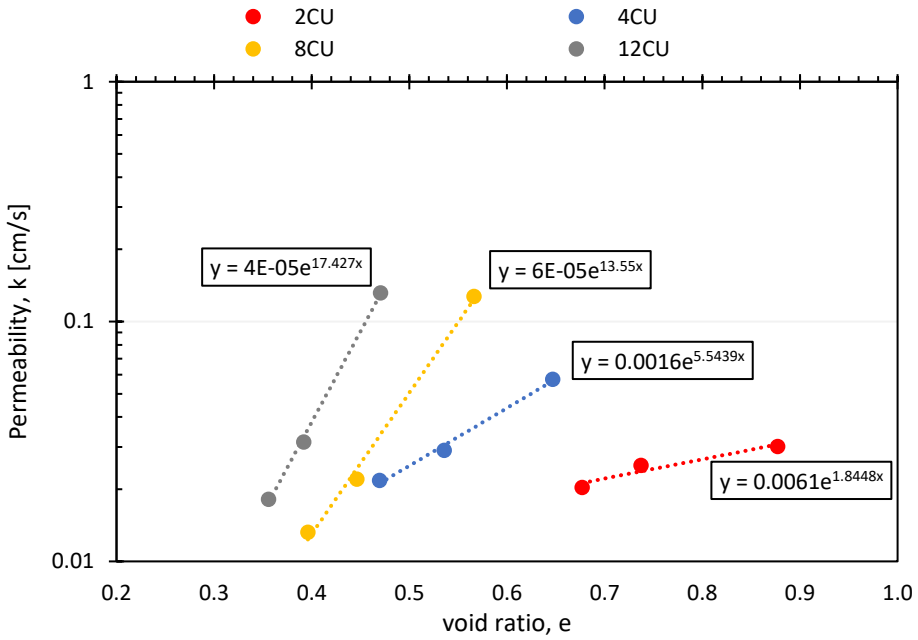

Figure S1. Permeability vs void ratio for each sand.

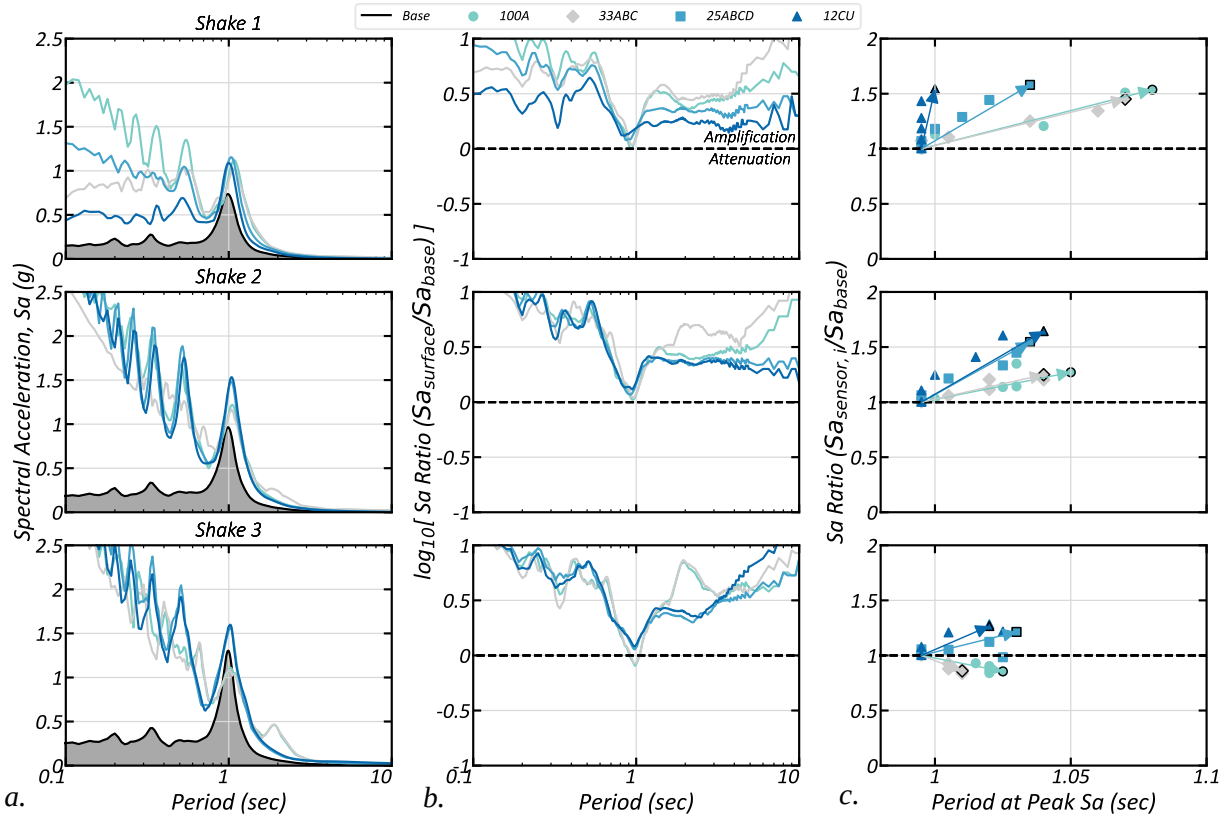

Figure S2. Acceleration time history records from shakes 1-3 for the midslope array, processed to obtain the: a. spectral acceleration (Sa) at for the surface sensor versus period, b. log of the ratio of the Sa of the surface relative to the base versus period to highlight amplification and attenuation, and c. Peak Sa ratio of each sensor in the array relative to the base versus period at the peak Sa, where the black outlined marker indicates the surface accelerometer and the arrow indicates the progression of sensors from the base to the surface.